Koushesh and Ritter
*Journal of Applied Volcanology* (2024) 13:9
https://doi.org/10.1186/s13617-024-00147-8

Journal of Applied Volcanology

RESEARCH

Open Access

# An adaptive 6-dimensional floating-search multi-station seismic-event detector (A6-DFMSD) and its application to low-frequency earthquakes in the East Eifel Volcanic Field, Germany

Konun Koushesh[1*] and Joachim R. R. Ritter[1]

**Abstract**

We introduce a seismic event detector that applies signal analysis in the time and frequency domains. Signals are searched for with matching coincidences at neighbouring recording stations in space and time. No a priori waveform information is needed for the Adaptive 6-Dimensional Floating-search Multi-station Seismic-event Detector (A6-DFMSD). It combines a short / long time average algorithm (STA/LTA), frequency range selection, energy envelope matching, and backprojection techniques to find a robust detection model. As a challenging test example, the new detector is tuned and applied to a dataset with five months of microearthquake ($ML < 2$) recordings in the East Eifel Volcanic Field (EEVF), Germany. There, both magmatic and tectonic earthquakes occur in a depth range between 3 km and 43 km. A6-DFMSD detected 4.3 times as many events as were already known and it discovered a previously unknown event cluster. After manual localization and classification of the events, we show that A6-DFMSD finds events of different origins: tectonic, magmatic, atmospheric, and anthropogenic. In particular, low-frequency (LF) earthquakes of magmatic origin with a complicated waveform coda are very well identified. We suggest that seismological networks monitoring local seismicity in similar target zones would benefit from the use of A6-DFMSD to allow the detection of a wide range of different seismic signals.

**Keywords** Automatic seismic event detection, Primary classification, Magmatic deep-low-frequency microearthquakes, Local seismological networks

## Introduction

Volcanic regions are known for a wide variety of seismic signals emitted from different sources connected with or activated by magmatism, tectonic stresses, and rock-fall processes (Sherburn et al. 1998; Neuberg 2011; Wassermann 2012; Naofumi et al. 2013). These signals substantially differ in frequency content and waveform compared to tectonic earthquake signals, and they can be emitted from a very shallow source position (like rock-fall events or magma oscillations in a crater) to very deep regions even from below the Moho discontinuity due to magma movements near initial melting processes. Thereby they cover a wide range of source intensities and activity rates (Ratdomopurbo and Poupinet 2000; Hidayat et al. 2000; Stroujkova and Malin 2001; Cusano et al. 2013; Malfante et al. 2018).

*Correspondence:
Konun Koushesh
konun.koushesh@kit.edu; koushesh@gmail.com
[1] Karlsruhe Institute of Technology, Geophysical Institute, Karlsruhe, Germany

One of the challenging issues in this regard is the detection of very weak signals and microseismic events (local magnitude $ML < 1$) in volcanic regions. Detection of the weak signals becomes even more challenging when we consider the two following common scenarios: (a) region of the study is newly covered by a local seismological network (b) the detection of new types of seismic sources (unknown waveforms) becomes a special goal for the local seismological monitoring.

In both cases, there is no a priori information specifying the target waveform characteristics to search for. On the other hand, the state-of-the-art high-performance seismic event detectors, like the template matching method (Ross et al. 2019), supervised machine learning methods (Perol et al. 2018), or some of the unsupervised machine learning methods (Yoon et al. 2015) need a priori estimates regarding the target waveform characteristics for training the algorithms.

In this work, first, we introduce a new detection routine in MATLAB called Adaptive 6-Dimensional Floating-search Multi-station Seismic-event Detector (A6-DFMSD) which does not require a priori knowledge of the target waveforms. To search for matching detections at neighbouring recording stations, it uses a homogeneous or, in the best cases, a 1-D layered velocity model, to find a detection model. Second, we evaluate the performance of A6-DFMSD by analysing a challenging seismological dataset. The test dataset includes five months of continuous recordings from the East Eifel Volcanic Field (EEVF), Germany, where earthquake signals of both tectonic and magmatic origins have been reported (Hensch et al. 2019). Subsequently, we manually pick the identified phases, localize and classify the detected events and compare them with the published event catalogues of two local seismological surveys (state seismological service of Rhineland-Palatinate and Bensberg Observatory, University of Cologne 2023) that monitor seismic activity in the region. We also compare our results with an internal event list provided by Hensch et al. (2019) which is focused on deep low-frequency (DLF) events in the EEVF. A comparison of the performance is provided regarding the detection of DLF events with the same test dataset between A6-DFMSD and the STA/LTA method (Allen 1978; Trnkoczy 2009) after tuning its parameters to DLF events.

Previous seismological and geodynamic studies on the EEVF (Fig. 1) suggested a deep-seated mantle plume system (Ritter et al. 2001; Ritter 2007; Kreemer et al. 2020) and a long-lived magma chamber beneath the Laacher See volcano (Wörner and Wright 1984; Schmitt et al. 2010) where the last big eruption occurred about 13 ky ago (Schmincke et al. 1983; Reinig et al. 2021). After the detection of the first two DLF events at depths of 40 km and 43 km on 18th and 22nd in Sep. 2013 (Stange et al. 2014), monitoring of the seismicity in the EEVF became an important scientific subject. To investigate microseismic activity in the region more closely, especially regarding DLF events, several temporal seismic stations were installed in between the few existing permanent stations in the region. This seismological experiment is called Deep Eifel Earthquakes Project - Tiefe Eifel Erdbeben (DEEP-TEE) and started in July 2014 (Ritter et al. 2024). Up to now, the DEEP-TEE seismic dataset contains almost ten years of continuous seismic records (more than 2.4 terabytes in volume) and the network has been reconfigured and continuously improved to achieve an optimum configuration regarding detection and location of seismic events.

Detection of LF events is more challenging than detection of tectonic events, because of their waveform complexity, diversity and often low signal-to-noise ratio. Although the observation of LF waveforms in records from volcanic areas can be related to the strong attenuation of the signals in the subsurface (Bean et al. 2014), this is not the case for the deep LF (DLF) events observed in EEVF. Here the corner frequency of the deeper LF events is often higher than for the shallower LF events (Hensch et al. 2019). This observation of higher frequencies from larger depths indicates that the unusual low frequencies of DLF earthquakes are not caused by any filter effects between source and receiver, e.g., due to shallow low velocity zones such as fluid reservoirs (Hensch et al. 2019). Anyhow, we use the frequency content as parameter for the detection.

In volcanic regions, the origin of LF events has been attributed to the growth and possibly resonance of fluid-filled cavities (Aki et al. 1977; Aki and Koyanagi 1981). Further modelling and numerical studies are reported in Neuberg et al. (2000). Waveform characteristics and spectral content of these signals depend on the source geometry, the location where the crack nucleates, and the acoustic properties of the fluid or embedding rocks. As a consequence, waveforms of these signals are more complex than those from purely tectonic sources. LF events in the EEVF occur in a wide depth range from ca. 8–43 km, whereas tectonic events in this region have only a source depth between ca. 3–15 km (Hensch et al. 2019). Below, we label as DLF those LF events whose sources are below the Moho (deeper than 29 km). The wide depth range spanned by the LF events in the EEVF influences and increases the waveform diversity: there is a large variability in S-P phase arrival times and often the phases (specially the P-phases) are strongly attenuated. Another factor, which is important regarding detection of the LF events, is the low magnitude of the events. In the EEVF the known LF events have very weak

magnitudes between 0.4 *ML* and 1.3 *ML*, except for two events with 1.7 *ML* and 1.8 *ML*. The related low-amplitude phases make the detection harder, especially during the day time when anthropogenic noise level increases strongly in the EEVF. Due to this background, the idea behind A6-DFMSD is to develop a robust search method which can cope with a wide frequency band, waveform diversity, and low phase amplitudes without the need for a priori waveform information.

In the next section, we explain the technical side of the method A6-DFMSD in accordance with the flow diagram in Fig. 2. Later in the discussion section we expand on the advantages, limitations and the capabilities of the method. A user manual of the detector is also provided besides the codes in GitHub (https://github.com/Koushesh/A6-DFMSD/tree/master) as the Supplementary file to explain more details. Since the codes are written in MATLAB, Signal Processing and Statistics Toolboxes are required to be installed in advance. The abbreviations used in this paper are listed alphabetically in Table 1.

## Method and parameterization

A6-DFMSD method and its philosophy are explained in the following subsections and Fig. 2:

- Input Parameters.
- Configuration of the Detection Model (CDM step).
- Detection Field preparation (DF preparation).
- Single Station Detection (SSD step).
- Multi-Station Detection (MSD step).

### Input parameters

A6-DFMSD is designed to detect the seismic signals which originate from a predefined seismic target zone (e.g., a volcanic field) and which are recorded by a local seismological network. For this reason, in addition to the three continuous seismic velocity records (Z: vertical, N: north-south, E: east-west), the following information is needed to construct a detection model:

(a) coordinates and codes of the seismological stations,
(b) a simple (homogeneous or layered) 1-D P- and/or S-wave seismic velocity model,
(c) a center location, a radius length for a target area, an upper and a lower depth for determining the event locations inside the target area. These data define a cylindric geometry of the target zone.

**Table 1** The alphabetically sorted abbreviation list

| Abbreviation | Meaning |
|---|---|
| 6-DFF | 6-Dimensional Floating-search Frame |
| A6-DFMSD | Adaptive 6-Dimensional Floating-search Multi-station Seismic-event Detector |
| CDM | Configuration of the Detection Model |
| DEEP-TEE | Deep Eifel Earthquakes Project - Tiefe Eifel Erdbeben |
| DF | Detection Field |
| DLF | Deep Low-Frequency |
| EEVF | East Eifel Volcanic Field |
| LF | Low-Frequency |
| MSD | Multi-Station Detection |
| SSD | Single Station Detection |
| STA/LTA | Short Time Average/Long Time Average amplitude |

### Configuration of detection model (CDM step)

A6-DFMSD uses the input information to construct a model and generates some outputs which later are used in DF preparation and MSD steps. The CDM step consists of the following sub-steps:

(a) Defining the upper and lower sides of a seismic target zone: synthetic source positions are distributed inside the circular bottom and top sides of a cylindric target zone, to cover the shortest and the longest raypaths. Figure 3a provides an exemplary top view of distributed synthetic source positions which are the same as in the application of this study (see Sect. on Test example and results).
(b) Calculating the P- and S-phase travel times ($T_p$ and $T_s$, respectively) for each individual combination of the synthetic sources and the recording stations: the local 1-D seismic P- and S-wave seismic velocity models, the synthetic source positions, the positions of the seismological stations and Snell's law are used for the ray path approximation.
(c) Obtaining sets of time limits for the search coherencies based on the potential travel times between the recording stations and possible source locations: these time limits are used in the MSD step when the seismic signals, which originate from the target zone, are discriminated from signals with source locations outside the target zone. In this part, A6-DFMSD calculates the relative difference in arrival time of the seismic phases between each pair of stations considering each synthetic source. Figure 3b and c, visualize these (exact-) time limits in dark blue and dark red bars for recording stations DEP02 and ABH, respectively. There, the light blue and light red bars indicate the exact-time limits after rounding up in respect with the window length "minStatisDur" explained in the second next paragraph (sub-step (e)). The detector takes the rounded-time limits instead of the exact-time limits while searching coherencies. This prevents to miss

the detection of the events at the edges of the time limits.

(d) For each station, the four closest stations are determined: this information is used to limit the search for coherencies in space in the MSD step. Figure 4a shows how the stations are grouped for the test example in this study.

(e) Estimation of an optimum time window (called "minStatisDur") for windowing seismic traces: minStatisDur is obtained by a statistical approach to estimate the typical half signal duration of the microearthquakes which are supposed to occur inside the target zone and are recorded at the seismological network.

#### Detection field preparation (DF preparation)

In A6-DFMSD, the distribution of recorded energy around the signal anomalies is taken as an attribute for searching coherencies. This is especially helpful to search for frequency-dependent signals, e.g., such as LF magmatic tremor. This part provides basic information to analyse the distribution of the recorded energy in different frequency ranges (here called signal classes). Such frequency-dependent signal classes are helpful for the detection of different type of signals with different frequency contents observed in volcanic regions (Chouet 1988; Neuberg 2011; Naofumi et al. 2013). For this purpose, each component of the continuous velocity records is decomposed into 29 narrow frequency bands (with a width of 1-Hz in our application) spanning the frequency range 1–30 Hz (Fig. 5b, c and d). We verify that choosing a narrower band width than 1-Hz adds artifacts to the data specially to the lower frequency part. Choosing a wider band width reduces the sensitivity of the method in extracting features of the signal anomalies. Following Eq. 1, the narrow-band seismic velocity traces are then converted to energy-proportional ($E^*$) narrow band traces. There, for each sample i of each narrow band j (with j running from 1 to 29) $E^*$is obtained by the summation:

$$E^*_{j,i} = Z^2_{j,i} + N^2_{j,i} + E^2_{j,i} \tag{1}$$

where $Z$, $N$ and $E$ are seismic velocity records of the three components of ground motion (Fig. 5e). The energy-proportional narrow bands are the unified measures of the ground motion. With this summation the whole recordable energy of the signals in each frequency band is taken into account. This prevents to miss the detection of polarized seismic signals.

In the next step, the energy-proportional narrow bands ($E^*_j$) are windowed (Fig. 5f). By windowing, we mean partitioning the data with a constant window length (routine minStatisDur) in the time domain and then taking the mean value of each partition for further analysis. The value for "minStatisDur" is obtained in the CDM step (see Sect. on CDM step). As results of this procedure, we obtain 29 windowed energy-proportional narrow bands called Detection Fields (DFs). The DF of each narrow band is indexed by j ($DF_j$).

#### Single station detection (SSD step)

For each recording station, signal anomalies are detected independently in different frequency ranges called signal classes. Each signal class is defined by two values denoting the upper and lower corner frequency of a desired frequency range in Hz. Depending on the corner frequencies of the signal classes, each signal class contains a bunch of certain DFs (Fig. 5f). A signal anomaly is detected when the signal to noise ratios exceed certain thresholds at all the DFs of a signal class. Similar to the STA/LTA (short / long time average amplitude) algorithm (Allen 1978), the threshold values vary depending on the amplitude value of each sample. For each sample i of a DF, a threshold is defined by the mean value of the amplitudes of the three samples before sample i (reference samples or noise part) plus the absolute mean deviation of the amplitudes of the reference samples multiplied by 0.7 (an empirical constant). This empirical constant can be varied to adjust the sensitivity of the detection.

As an example, in Fig. 5g, the detection of a signal anomaly in a signal class is presented (signal class 6 among the total 11 predefined signal classes). Based on the detector logic, sample i (red dot) is detected as a signal anomaly, because the amplitude values at sample i have a higher value than the defined thresholds (blue dashed lines) at all DFs of the signal class. In Fig. 5 the reference samples are shown by the green dots right before the sample i.

For each signal anomaly, which is detected in a signal class, a unique set of six parameter values is saved as the labels of the signal anomaly. These six parameter values are:

- station code: implicitly, the latitude and longitude of the station location.
- sample number (i) of the detection point: representing the detection time.
- signal class ($n$): which is defined by the upper corner ($j_2$) and the lower corner ($j_1$) of a frequency range in Hz.
- variation coefficient ($\Lambda$) of the DFs at the detection point i in the signal class $n$: this is obtained from Eq. 2 and implicitly represents the distribution status of the recorded energy at the point of detection in the corresponding signal class. $\Lambda$ is indeed equal to standard

deviation of the DFs amplitudes in the signal class $n$ at the detection point i, divided by mean value of the DFs amplitudes ($\mu$) in the same signal class $n$ and at the same detection point i. The $\mu_{n,\,i}$ used in Eq. 2 is obtained by Eq. 3.

$$\Lambda_{\,n,i} = \frac{\sqrt{\frac{1}{j_2-j_1+1}\sum_{j=j_1}^{j_2}\left(DF_{j,i} - \mu_{\,n,i}\right)^2}}{\mu_{\,n,i}} \tag{2}$$

$$\mu_{\,n,i} = \frac{1}{j_2 - j_1 + 1}\sum_{j=j_1}^{j_2} DF_{j,i} \tag{3}$$

- a value called "sigClasPower ($\Gamma$)": which implicitly represents the amplitude ratio of the recorded energy in the signal class $n$ at the detection point i relative to the reference samples (noise part). $\Gamma$ is obtained from Eq. 4. It is equal to the result of the division of two values: the numerator is the mean value of the DFs amplitudes in the signal class $n$ at the detection point i ($\mu_{n,\,i}$) minus the mean value of the DFs amplitudes of the reference samples (in Fig. 5h, this is equal to the length of the red line), and the denominator is the mean absolute deviation of the mean values of the DFs amplitudes of the reference samples (in Fig. 5h, this is equal to the length of the blue line). $M_{n,\,i}$ which is used in Eq. 4, is obtained by Eq. 5 and is equal to the average of the mean value of the DFs amplitudes of the reference samples of detection point i in the signal class $n$.

$$_{n,i} = \frac{\mu_{\,n,i} - M_{n,i}}{\frac{1}{3}\sum_{i=i-3}^{i-1}\mu_{\,n,i} - M_{n,i}} \tag{4}$$

$$M_{n,i} = \frac{1}{3}\sum_{i=i-3}^{i-1}\mu_{\,n,i} \tag{5}$$

**Multi-station detection (MSD step)**

A signal anomaly detected at a station is listed as an event only if a certain number of coherent signal anomalies are found at other stations. This is similar to the phase association part in other known techniques. Here searching coherent signal anomalies is done by applying a 6-Dimensional Floating-search Frame (6-DFF). Depending on the labels of each signal anomaly (the unique set of six values), 6-DFF sets specific search ranges and limits accordingly. In this way, labels of each signal anomaly are taken as reference, based on the content of the reference labels (we use the phrase "reference labels" to indicate labels of the signal anomaly which are taken as reference):

a) the coherency search in space is limited to the four closest stations (called "orbit stations"). This supports the principle that the direct waves of the local events arrive earlier at stations closer to the source than at the more distant ones. As a result of applying such a coherency search limit in space, the number of false detections was remarkably reduced in our tests.
b) the coherency search in time is limited to a certain time window around the time sample in the reference label. The time window limits are unique and differ from station to station depending on the relative position of the reference and orbit stations in relation with the position of the target zone. The time and space limits, which are applied in this step, are already determined in the CDM step.
c) the coherency search in a signal class is limited to the corresponding signal class of the reference label.
d) the coherency search in sigClasPower ($\Gamma$) is limited to the labels having a sigClasPower value more than 2.
e) the coherency search with a variation coefficient ($\Lambda$) for DFs is limited to a border value around the variation coefficient of the DFs of the reference label. This border value (b) is obtained by empirical Eqs. (6) and (7):

$$b(\Lambda) = 1.6^{-(\Lambda + a)} \tag{6}$$

$$b(\Lambda) = c \times \Lambda + d \tag{7}$$

$a$ in Eq. 6 is a constant which can take a minimum value of 2.7. Following our test runs to minimize the ratio of false detections to the total number of detections, we found values 2.7 and 2.9 are suitable choices for $a$ when the upper border of the target zones is 3 km depth and 30 km depth, respectively. The parameters $c$ and $d$ in Eq. 7 are constant values and after trial and error, we found the best values to be 0.306 and 0.113, respectively, to minimize the ratio of false detections to the total number of detections. This may differ for other applications.

In Eq. 6, the coherency search gets a wider border when $\Lambda$ at the reference label has smaller values. In contrast, in Eq. 7 the coherency search gets a wider border when $\Lambda$ at the reference label has bigger values. The borders determined by Eq. 6 are suitable for the detection of the signals which have less fluctuations in the amplitude of their frequency spectra around their dominant frequencies. This was the case for tectonic-type events in our study. In contrast, the borders determined by Eq. 7 are suitable for detection of the signals which have large fluctuations in the amplitude of their frequency spectra around

their dominant frequencies, like LF type events. Further explanations are provided in the Supplementary file (Sect. 1.5.2: Eqs. 6 and 7 and, Figs. S5 and S6). Figure 4b shows the relationship between $b$ and $\Lambda$ while detecting events in different signal classes in the differently defined seismic target zones in our test example.

Following a) – e), if two or more coherent signal anomalies are found at other stations (while passing through all the above 6-DFF conditions), the routine accepts the referenced signal anomaly as an event which originated from the seismic target zone. It is then written into the detection list. The detection list contains the following information regarding each detection:

- date, arrival time and duration of the event in UTC.
- codes of the stations having coherent labels.
- the signal class of the reference label.

While manually checking the detection outputs, the two latter information helps users to select events based on their dominant frequeancy content and/or based on the stations where the signal of the event was detected.

## Test example and results

We apply the A6-DFMSD routine to study a period with microseismicity in the EEVF (Fig. 1). We select 5 months (October 1, 2017 - February 28, 2018) of continuous seismic records of the DEEP-TEE recording stations. In this time period, the recording equipment consisted of four broad-band STS2 (120 s) sensors and one short period Lennartz 3-D (1 s) at the mobile recording stations. At the permanent stations one Nanometrics sensor (Trillium Compact 120 s), one STS2, and seven short period sensors (1 s) including Mark L4 and LE3-D sensors were used. There were strongly varying noise conditions, because of traffic

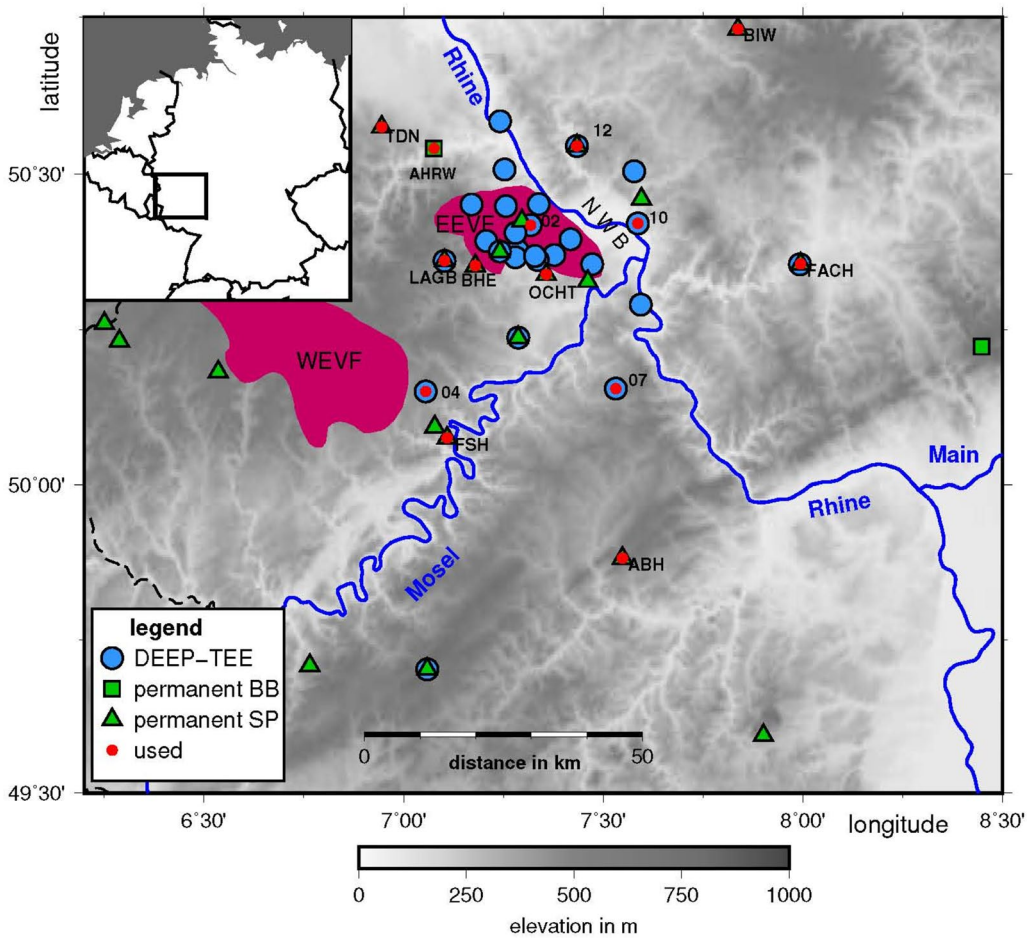


**Fig. 1** Location of the Quaternary East and West Eifel Volcanic Fields (EEVF, WEVF, reddish areas) with the seismological stations of the DEEP-TEE experiment. Green symbols indicate permanent recording stations (BB: broadband, SP: short-period), blue symbols are temporary stations; a red dot indicates stations used in this study. NWB: Neuwied Basin. The inset shows the position of the study region (square) in Germany

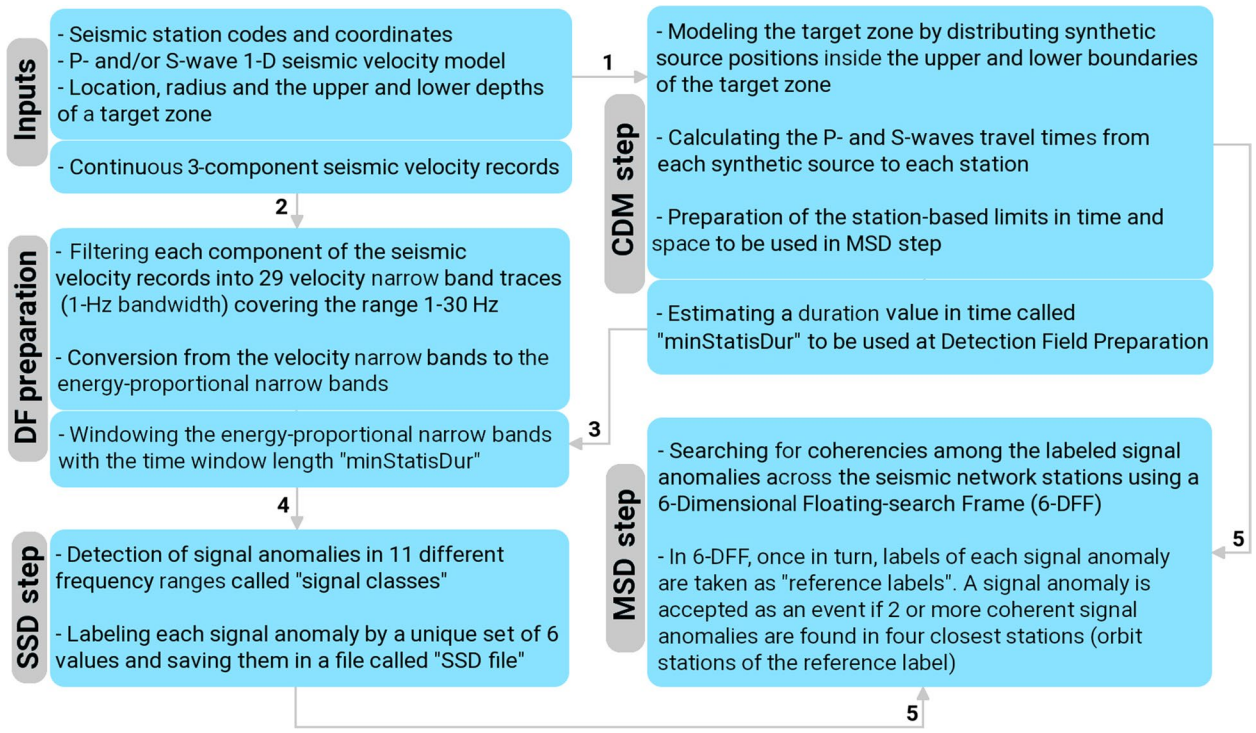


**Fig. 2** Overview on the major steps of A6-DFMSD: Inputs, Configuration of the Detection Model (CDM step), Detection Field preparation (DF preparation), Single Station Detection (SSD step), and Multi-Station Detection (MSD step)

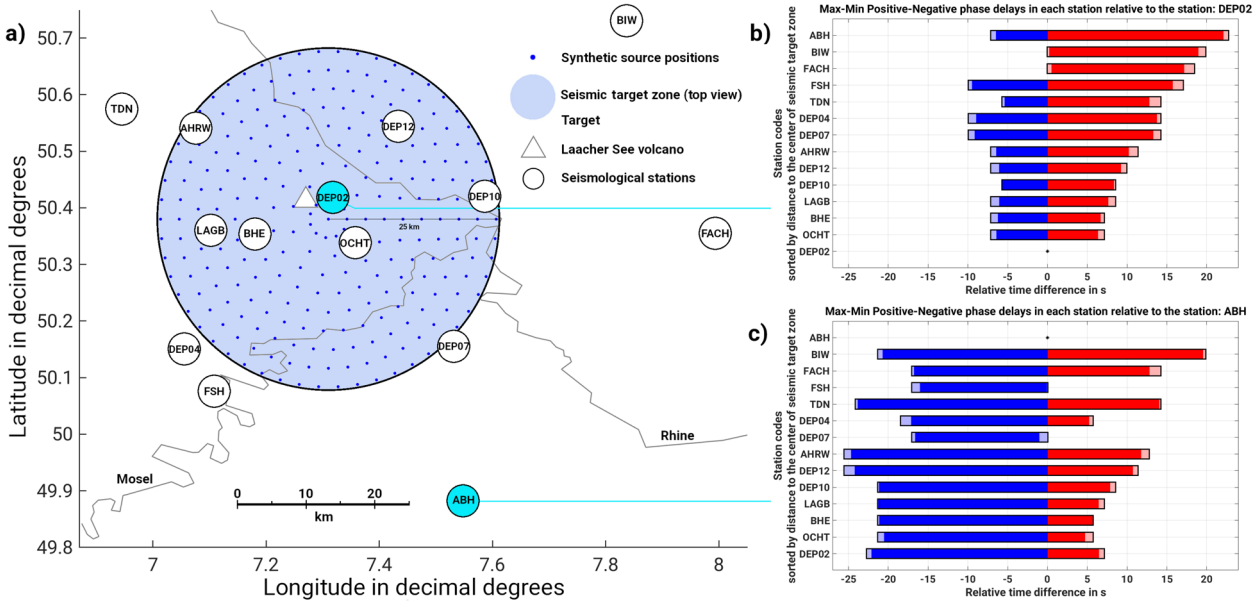


**Fig. 3** Configuration of a detection model (CDM step) in association with the test example in the EEVF (Fig. 1). **a** station locations and top view of the seismic target zone considered in this study. Each small blue dot is considered as a seismic source and the travel times for the first P- and S- phase arrivals are calculated for each source-station pair. **b** subset of calculations to find the station-wise detection limits in the time domain. It is indicated how long before (in light blue) and/or after (in light red) the detection of a seismic phase at station DEP02 the routine searches for coherent seismic signals in the records of the other stations. **c** the same b), but here the time differences are obtained relative to the recording station ABH. Note: in b) and c) the dark blue and dark red bars denote the exact-time limits, and the light blue and light red bars indicate the exact-time limits after rounding up in respect with the window length "minStatisDur"

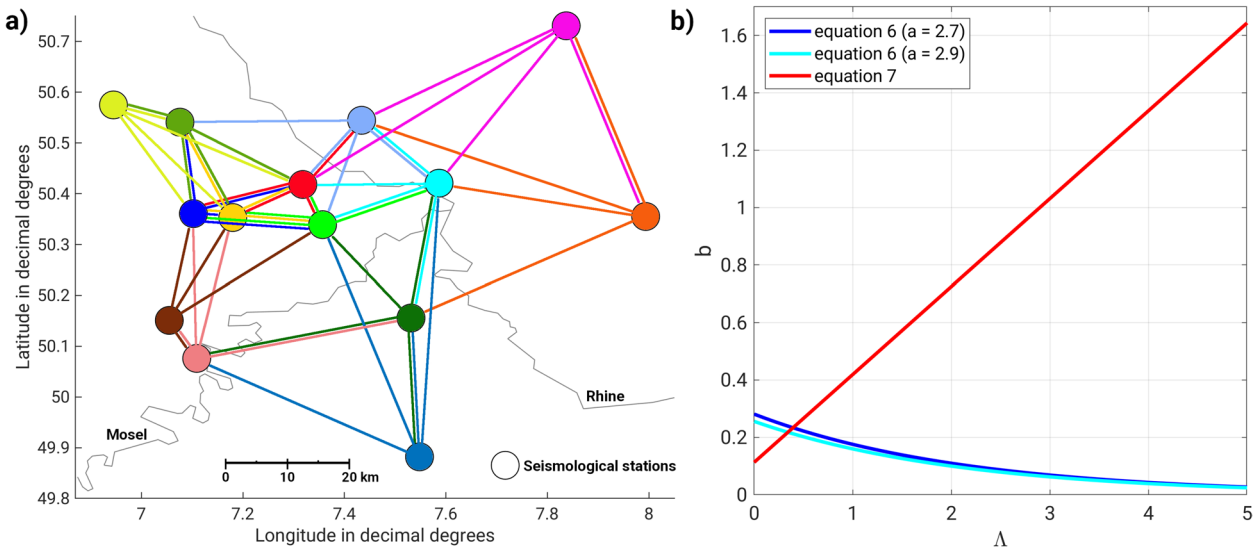


**Fig. 4** **a** Station locations and their mutual relationships while searching and connecting coherent signals in the Multi-Station Detection step (MSD step). For each station, the coherency search is limited to a radial distance in which only the four closest stations are involved. Here, each station is plotted with a specific color and the corresponding four nearest stations are linked to it with the same color, (**b**) during the MSD step, vicinities for the coherency search for the variation coefficient of the DFs are determined using empirical Eqs. (6) and (7). Here this relationship is plotted in blue (dark and light) for Eq. (6), and in red for Eq. (7). The dark blue line shows this relationship while searching for tectonic and volcano-tectonic events (signal classes higher than 3) in the shallower zone (3–30 km depth), and the light blue line shows this relationship for the detection of possible events in the deeper zone (30–50 km depth). The red line indicates this relationship while searching for LF events (signal classes less than 4, see Sect. on SSD step) in both seismic target zones

and industrial activity (Ritter et al. 2024). Table 2 lists the properties of the DEEP-TEE recording stations in more details plus the missing data status for each station within the five-month long selected time period.

To assess the performance of A6-DFMSD regarding the detection of DLF events, we compare the results of A6-DFMSD with the results of the STA/LTA routine (Allen 1978). The events detected by both methods are checked by a visual inspection of the waveforms, then they are manually localized and classified (as DLF, tectonic etc.) according to their waveform properties. We use the minimum 1-D layered velocity models KIT5 for *vp* and vs. (Ritter et al. 2024) and the routine VELEST (Kissling et al. 1994) to localize the events with at least six picked seismic phases. To check whether the events detected with A6-DFMSD are newly discovered events (or not) in comparison with the published local seismicity catalogues, we also cross-check each event with the event catalogues provided by the state seismological service of Rhineland-Palatinate (2023) and Bensberg Observatory, University of Cologne (2023). Both institutions regularly monitor and report seismic activity in the study region. In addition, an internal event list from Hensch et al. (2019) is used which specifically lists DLF earthquakes of magmatic origin. Since A6-DFMSD is configured to detect events from a certain seismic target region, we summarize the final results in association with this target region. In the two following sections, we explain how the parameters for both A6-DFMSD and STA/LTA method are chosen, afterwards we

(See figure on next page.)

**Fig. 5** Examples for Detection Field preparation (DF preparation) and Single Station Detection step (SSD step). **a** three-component band-pass filtered (1–30 Hz) ground motion velocity of a microearthquake recorded at station AHRW, **b**), **c**), and **d**) decomposition of each component Z, N, and E by filtering with 29 1-Hz-wide frequency bands, **e**) conversion of the ground motion velocity in each frequency band into energy-proportional narrow bands following Eq. (1), **f**) traces in e) are windowed to prepare the Detection Fields (DFs), **g**) detection status of a signal anomaly at the sample i in the signal class $n=6$ is shown. The red dot (sample i) is detected as a signal anomaly because the amplitude values at sample i have a higher value than the specific thresholds defined by reference samples (three green dots). The bold line is the stack of DFs of the signal class 6 (DFs from $DF_8$ to $DF_{16}$), **h**) close-up view of the stacked trace in g). Value of sigClasPower ($\Gamma_{6,i}$) at sample i in signal class $n=6$ can be illustrated as ratio of the length of the red line to the blue line. The technique used for detecting signal anomalies (g and h) is partly similar to the STA/LTA method with a very sharp criterium (window length in the LTA part is only three times longer than in the STA part)

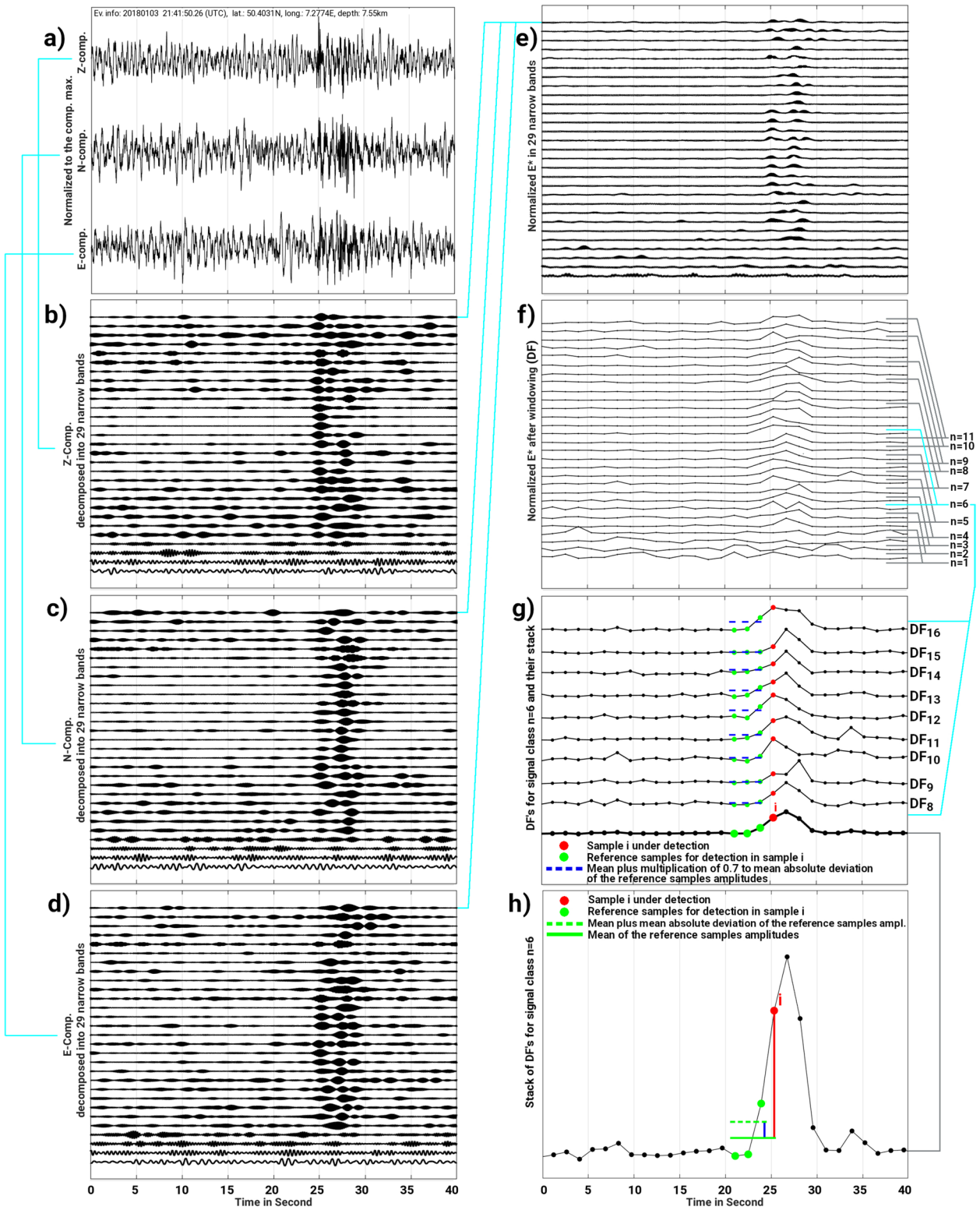


**Fig. 5** (See legend on previous page.)

**Table 2** The DEEP-TEE recording stations used in this study. The column indicated by "Missing" gives the number of the days without data. The column indicated by STA/LTA marks the stations used in STA/LTA test by a "+" and the not used by a "-"

| Network Station code | Lat. in degrees | Lon. in degrees | Elev. in m | Sensor type | Sampling rate in Hz | Missing Data in days | STA/LTA |
|---|---|---|---|---|---|---|---|
| KB.DEP02 | 50.4181 | 7.3181 | 310 | STS-2 120 s | 100 | 0 | + |
| KB.DEP04 | 50.1509 | 7.0550 | 455 | STS-2 120 s | 100 | 0 | + |
| KB.DEP07 | 50.1556 | 7.5312 | 428 | LE-3D 1 s | 100 | 0 | + |
| KB.DEP10 | 50.4208 | 7.5865 | 164 | STS-2 120 s | 100 | 0 | - |
| KB.DEP12 | 50.5447 | 7.4337 | 295 | STS-2 120 s | 100 | 0 | + |
| LE.OCHT | 50.3387 | 7.3575 | 140 | LE-3D 1 s | 100 | 0 | + |
| LE.LAGB | 50.3608 | 7.1007 | 372 | Trillium 120 s | 100 | 0 | + |
| LE.FSH | 50.0760 | 7.1090 | 350 | LE-3D 1 s | 100 | 59 | - |
| LE.ABH | 49.8820 | 7.5480 | 618 | Mark L4 1 s | 100 | 0 | - |
| LE.FACH | 50.3563 | 7.9938 | 110 | LE-3D 1 s | 100 | 0 | - |
| LE.BIW | 50.7308 | 7.8373 | 310 | LE-3D 1 s | 100 | 23 | - |
| GR.AHRW | 50.5419 | 7.0760 | 180 | STS-2 120 s | 100 | 17 | + |
| NH.BHE | 50.3530 | 7.1800 | 290 | Mark L4 1 s | 200 | 0 | + |
| NH.TDN | 50.5750 | 6.9450 | 350 | Mark L4 1 s | 200 | 0 | - |

explain the summarized results in Tables 4 and 5, where A6-DFMSD is compared with the three local seismicity catalogues and with STA/LTA results, respectively.

#### A6-DFMSD parameter setting

Concerning the variety of the observed signals in the EEVF (Hensch et al. 2019), we adapt the control file of A6-DFMSD to search for a wide range of signals. It covers the frequency ranges typical for the observed DLF events (ca. 1–8 Hz) and of the tectonic microseismic events (> 10 Hz) by considering eleven frequency ranges as a part of the search limits (eleven signal classes). The lower and higher frequency borders of these eleven signal classes (1–11) are: [1 5] Hz, [2 7] Hz, [3 9] Hz, [4 11] Hz, [6 14] Hz, [8 17] Hz, [10 20] Hz, [12 23] Hz, [13 25] Hz, [15 28] Hz, and [16 30] Hz. We set the centre of the seismic target region to the midpoint between the epicentral area of the 75 reported DLF events (Hensch et al. 2019) and the centre of the Laacher See crater (Fig. 1), with a radius of 25 km (Fig. 3a). The control file parameters are adjusted to search for events which possibly occur in two different depth zones: zone 1 is limited between 3 km and 30 km depth and zone 2 is limited between 30 km and 50 km depth.

#### STA/LTA parameter setting

The STA/LTA parameters are tuned to reach the most appropriate performance regarding the detection of the DLF events, because these are the main goal of our research study. In this regard, concerning the seismic noise conditions, at first, we select the eight quietest and closest recording stations to the target region out of the total of 14 available stations in the DEEP-TEE dataset. The noise level conditions were determined with a probabilistic power spectral density analysis (Ritter et al. 2024). Since the DLF events of the EEVF have a dominant frequency range of 1–8 Hz (Hensch et al. 2019), we filter the recordings in the same frequency range with a band-pass filter before using STA/LTA detector. Then, as input for STA/LTA, the band-passed filtered records of each station are converted to the energy-proportional records using Eq. 1. The results of the station-wise STA/LTA detections are then collected into one detection list and compared within a 7 s time window for coincident detection. We choose a time length of 7 s in accordance with the observation of the typical DLF events in EEVF. After testing different sets of STA/LTA parameters, we select the most appropriate ones (Table 3) for which the number of false detections reaches a minimum while none of the DLF events is missed which are listed in the outputs of A6-DFMSD and in the local seismicity catalogues.

**Table 3** STA/LTA parameters for detecting DLF events

| Parameter | Choice |
|---|---|
| STA window length in s | 2 |
| LTA window length in s | 15 |
| Triggering STA/LTA threshold | 2 |
| Detriggering STA/LTA threshold | 1.5 |
| Time window for clustering events for an integrated detection list in s | 7 |

### Detection summary

Table 4 shows the results of A6-DFMSD in comparison with the merged three menioned seismicity catalogues. We provide two sets of results for comparison. One is generated in a high sensitive mode and another one in a low sensitive mode for the detection of DLF events. In the high sensitive mode, we select a subset of the events in the detection lists that are detected by at least six stations out of a total of 14 stations. In the low sensitive mode, we select a subset of the events in the detection lists that are detected by at least seven stations out of 14 stations. For both modes, while searching DLF events within the detection lists of A6-DFMSD, we only select the event list corresponding to the target depth of 30–50 km (zone 2) and the events whose initial frequency classes are labelled between 1 and 3, covering the frequency range 1–9 Hz. To select tectonic events and possibly volcano-tectonic events, we take detections from both depth zones, 3–30 km and 30–50 km. Since volcano-tectonic type of events had never been reported in EEVF, we find it worthful searching this type of event in both ranges of depths in target region. To account for the higher frequencies of tectonic and possibly volcano-tectonic earthquakes compared to magmatic events (Hensch et al. 2019) we selected the detections with initial frequency classes between 4 and 11, covering the frequency range 4–30 Hz. In addition, we select that part of the detection lists in which the events are detected by at least five stations out of 14 stations. This selection, which is the result of some trial-and-error testing, controls the efficiency of the work regarding the ratio of false detections to the total number of detections. The outputs are analysed into two main categories: events inside and events outside of the target region.

As summarized in Table 4 and as far as the information of the public event catalogues allows, in general A6-DFMSD detects about 4 times more natural events which can be classified by their source type as DLF, tectonic and volcano-tectonic events. In Sect. on Event classification, we explain the characteristics of each type of the observed events in more detail. Comparing detection results of the high sensitive mode with the low sensitive mode shows a minor difference in quantity. Relative to the low sensitive mode we get 13% more events and 33% more false detections in the high sensitive mode.

With DLF event detection as a target, the low sensitive mode misses one DLF event which might be important for observatories. In Fig. 6a and b, seismicity maps of the target region are plotted before and after applying A6-DFMSD. Numbers of both, tectonic and DLF events, increase using A6-DFMSD. Especially, the increase of detected DLF events is important, since they are hard to find and their occurrence is a unique feature in Central Europe especially below the Moho at more than 29–30 km depth (Hensch et al. 2019). In addition, a new cluster of tectonic activity appears which has not been reported yet. This cluster of events is located around 50.3 °N, 7.3 °E (close to the village Polch) and it is highlighted by an orange circle in the map (Fig. 6b).

In Table 5, we compare the results of A6-DFMSD with the STA/LTA method. Here, we focus on the performance of the methods in detection of DLF events. For each method we provide two sets of outputs: the high sensitive and the low sensitive sets. For comparison of the methods, first, we investigate which output sets are generated in a higher efficiency and then compare the most efficient sets with each other. For the STA/LTA method, the first output set (A) is the high sensitive set and includes the events that are detected by at least five stations out of the eight chosen stations. The second output set (B) is the low sensitive set and includes the events that are detected by at least six stations out of the eight

**Table 4** Comparing the events in a merged list of three local seismicity catalogues with the detection results of A6-DFMSD. Here, A6-DFMSD is adjusted to detect all type of events

| | Event Type | Merged 3-Catalogues | A6-DFMSD | |
|---|---|---|---|---|
| | | | high sensitive mode | low sensitive mode |
| Inside the target region | DLF | 3 | 13 | 12 |
| | quarry blast | -- | 111 | 107 |
| | tectonic | 85 | 364 | 364 |
| | volcano-tectonic | 0 | 1 | 1 |
| Outside the target region | quarry blast or tectonic | not comparable | 1153 | 1046 |
| Number of false detections | | -- | 606 | 456 |
| Total number of detections | | -- | 2248 | 1986 |
| Ratio of false detections to total number of detections | | -- | 27% | 23% |

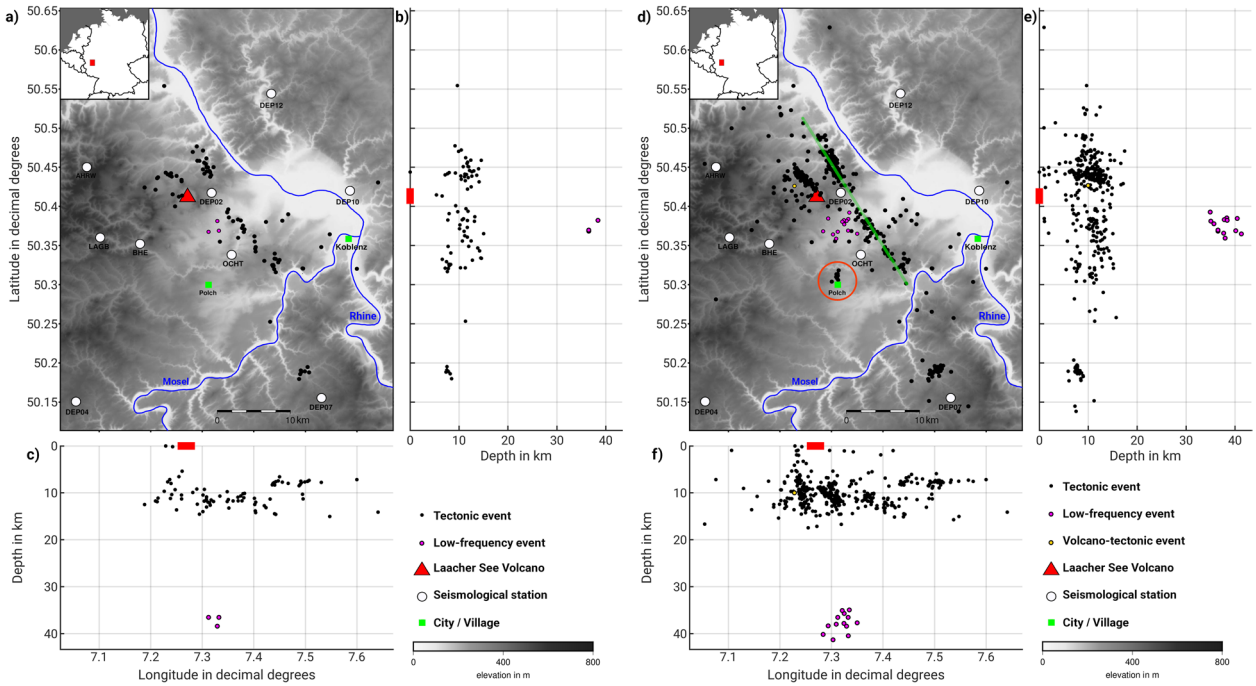


**Fig. 6** Seismicity map of the East Eifel Volcanic Field (EEVF) for the period between 1 Oct. 2017 and 28 Feb. 2018. a), b) and c) hypocenters of 88 microearthquakes known before applying A6-DFMSD. These events are already listed at least by one of the local seismological services: state seismological service of Rhineland-Palatinate (2023), Bensberg Observatory, University of Cologne (2023) or by Hensch et al. (2019). d), e) and f) hypocenters of 378 microearthquakes detected after applying A6-DFMSD. The green line shows the trend of the active Ochtendung fault zone, and the orange circle indicates the location of a newly discovered seismic cluster near the village Polch. Note: ten new DLF events (in purple) were discovered in the uppermost mantle

**Table 5** Comparing the detection results of STA/LTA with A6-DFMSD. Parameters of both methods are adjusted for detecting DLF events. Set A: detections by at least five out of eight chosen stations, set B: detections by at least six out of eight chosen stations, set A´: detections by at least six out of 14 available stations, set B´: detections by at least seven out of 14 available stations

| | **Event Type** | **STA/LTA** | | **A6-DFMSD** | |
|---|---|---|---|---|---|
| | | set A | set B | set A´ | set B´ |
| Inside the target region | DLF | 13 | 12 | 13 | 12 |
| | quarry blast | 101 | 84 | 98 | 94 |
| | tectonic | 81 | 46 | 3 | 3 |
| | Volcano-tectonic | 0 | 0 | 0 | 0 |
| Outside the target region | quarry blast or tectonic | 836 | 354 | 829 | 722 |
| Number of false detections | | 840 | 103 | 227 | 80 |
| Total number of detections | | 1871 | 599 | 1170 | 911 |
| Ratio of false detections to total number of detections | | 45% | 17% | 19% | 9% |

chosen stations. For A6-DFMSD, the first output set (A´) is the high sensitive set and includes the events that are detected at least by six stations out of all the 14 available stations. The second output set (B´) is the low sensitive set and includes the events that are detected by at least seven stations out of all the 14 available stations. Similar to Table 4, we select the events from the A6- DFMSD detection list which are generated for the target depth of 30–50 km and events whose initial frequency classes are labelled between 1 and 3, covering the frequency range of 1–9 Hz.

### *Comparison of set A with set B*

Considering the goal of detection, which is on DLF events inside the seismic target zone, the major difference is in connection with the number of tectonic

events (as unwanted type of detected event) and number of false detections. The results show that the high sensitive set (set A) includes 1.8 times more tectonic events along with 8.1 times more false detections relative to the low sensitive set (set B). This suggests that the low sensitive mode detects DLF events in a more efficient way using STA/LTA.

#### *Comparison of set A´ with set B´*

with the same criterium used for comparison of set A with set B, the only major difference between sets A´ and B´ is concerning the number of false detections. The high sensitive set (set A´) includes 2.8 times more false detections relative to the low sensitive set (set B´). This suggests that the low sensitive mode detects DLF events in a more efficient way using A6-DFMSD.

#### *Comparison of set B with set B´*

in both sets the same number of DLF events are detected. Set B, generated by STA/LTA, contains 1.3 times more false detections than set B´ generated by A6-DFMSD. Although the goal of both methods is the detection of DLF events, in set B 46 tectonic events are found which is 15.3 times more than in set B´. This shows how the designed automatic classification by A6-DFMSD filters out irrelevant types of events, as far as the dominant frequency of the events is located in a specific band of the frequency spectra. The total number of quarry blasts inside the target region in set B (84) and set B´ (94) is in the same order for both methods but the number of quarry blast / tectonic events outside the target region is 2 times more in set B´ compared to set B. Since these types of events have similar characteristics with DLF events, partly in the time domain (waveforms) and mostly in the frequency domain, an increase in detection of them is reasonable and predictable. This may be interpreted as higher sensitivity for detection of DLF events by A6-DFMSD in comparison with STA/LTA. Comparing the ratio of false detections to the total number of detections indicates that A6-DFMSD with set B´ (9%) is 1.9 times more efficient than STA/LTA with set B (17%), with respect to detection of all meaningful type of events (even while both methods are tuned for the detection of DLF events of a certain seismic target zone). 52% of false detections in set B and 23% of false detections in set B´ are multiple detections of same event (false positives).

### Event classification

In the framework of the test example and in accordance with the definitions by Malfante et al. (2018), Wassermann (2012) and Neuberg (2011), we manually classify the detected natural microseismic events of the seismic target region. Figure 7 summarizes the typical events detected during the five months of analysis by providing records of the vertical components of the events plus their corresponding spectrograms. Below in the discussion section, we present more observations regarding a diverse set of signals detected by A6-DFMSD while applying it on the DEEP-TEE dataset within a longer time period than for the test example.

#### *Tectonic events*

the frequency content in the ground motion velocity records of these signals is limited between 5 Hz and 40 Hz. The waveforms contain clear P- and S-phases highly affected by the double couple source mechanisms. As a general property, the duration of the signals and dominant frequency content in this event class are controlled by the magnitude of the event. A larger magnitude leads to a wider frequency content including lower frequencies and a longer duration of the signal. In some cases, we observed a longer signal duration of the tectonic events which is not only controlled by the magnitude but also by the source activity rate. In such cases, several tectonic-type events occurred within a short time window in such a way that phases of the first event are partly or completely covered by the phases of the second event and so on. The detected microseismic tectonic events, within the five months study period, had a minimum signal duration of less than 10 s at the surface considering the closest recording station to the epicentre ~ 5 km (Fig. 7a and b).

#### *Volcano-tectonic events*

the frequency content in the velocity records of this type of signals is limited between 4 Hz and 15 Hz. The waveforms contain clear P- and S-phases affected by a kind of radiation pattern (observations from different station-source back azimuths show different phase amplitudes and polarity). It is noticeable that, within the time period of the test example, only one event (Fig. 7c) could be found in this class. The observation of only a single volcano-tectonic (VT) event is in the contrast with the definition suggested by Wassermann (2012), where deep VT events are characterized by their frequent occurrence as swarms. The source of our VT event is located at a depth of 9.4 km with an epicentre close to the one of the $CO_2$ gas emission points (Gal et al. 2011) in the region. The minimum signal duration recorded on the surface is less than 10 s. This event was only detected by A6-DFMSD and was not listed in the three local seismological catalogues.

#### *Low-frequency events (LF)*

in general, LF events in the EEVF are quite diverse and their frequency content is mostly between 1 Hz and

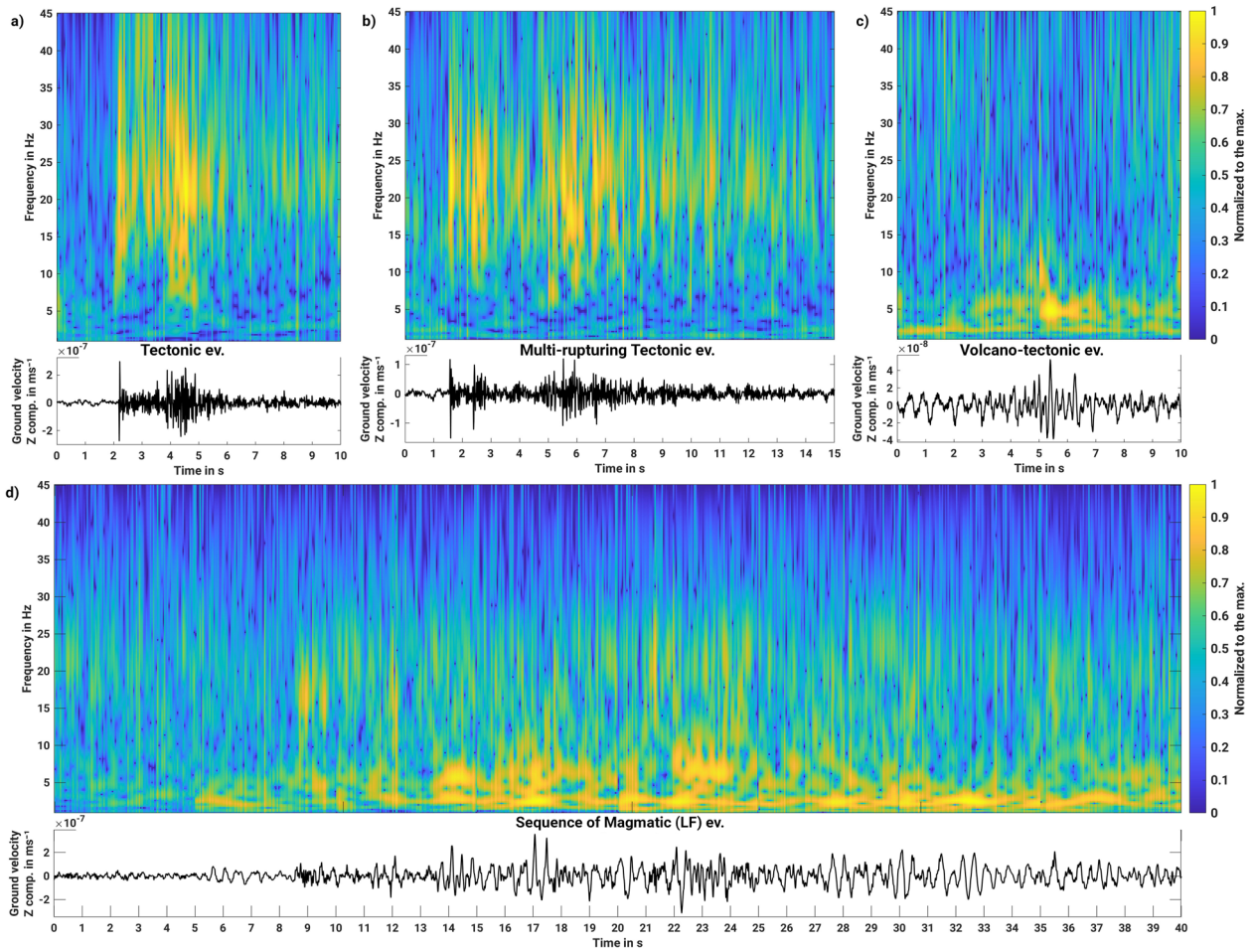


**Fig. 7** Waveform examples (ground motion velocity, vertical component) and their corresponding spectrogram, a) tectonic event, record since 2018-01-31T22:48:27.00 UTC at DEP12, b) multi-rupturing tectonic event, record since 2018-01-06T23:09:21.50 UTC at DEP12, c) volcano-tectonic event, record since 2018-02-18T02:01:46.00 UTC at LAGB, and d) low-frequency (LF) event, record since 2017-10-16T22:02:34.00 UTC at DEP12. All events occurred inside the seismic target region between 1 Oct. 2017 and 28 Feb. 2018

10 Hz. However, the higher frequency part of the signals has much smaller amplitudes than the lower frequency part. For this reason, we assign the LF class to this type of signals rather than other existing defined classes (e.g., hybrid). Most of the LF events are characterized by emergent phase arrivals and a much longer coda compared to the tectonic earthquake recordings, that is possibly due to the source mechanism of oscillating fluids in a crack (e.g., Chouet 1988; Neuberg et al. 2000). Except for a few sequences with a high source activity rate and hence overlapping waveforms, S-waves are well identifiable for the remaining LF events. Sometimes unusually deep hypocentres are found down to more than 40 km depth, which is well below the brittle-ductile transition at ca. 15 km depth (see depth distribution of the tectonic events Fig. 6). Therefore, *ts - tp* differential arrival times are longer than for tectonic events and P-waves of LF events are often attenuated along the long ray path. Within the test example time period, we detected six sequences of DLF events including overall 13 events. In comparison only one of these sequences with three events had already been listed in the catalogues of the local observatories. In Fig. 7d, a waveform example of the typical DLF events detected within the time period of the test example is plotted. It shows the occurrence of a sequence with several sub-events.

## Computational aspects

For the test example, the computational time for detection for each day (24 h of continuous recordings) takes ca. 75 min on a standard PC (using one core CPU – 3.3 GHz system) with on average 14 recording stations involved for each day. Each station has three-component records with a sample rate of 100 Hz, except for two stations BHE and TDN with a sample rate of 200 Hz. Detection is done simultaneously for searching events in two

seismic target zones with different depth ranges. The signals were searched in eleven frequency classes. Since our A6-DFMSD code in MATLAB is not yet written in parallel form, there is a potential for speeding up the detector in future works. The most time-consuming part of detection is the SSD step, specifically where the signal anomalies are detected and labelled for each signal class. Beside rewriting the code in a parallel form, considering preallocation memories for the defined arrays and reducing the number of nested loops could further optimize the code.

## Discussion

Detection of very weak earthquake signals ($ML < 1$) is a challenging issue in the presence of background seismic noise. A6-DFMSD routine provides a new way to detect signals emitted from a certain target region by analysing the records of the seismic stations located not only inside the target region, but also outside the target region where possibly the noise level is lower. A special feature is the high sensitivity for signal frequency that can be advantageous, if a specific frequency range characterises a type of seismic waves – a typical case in volcanic environments. As it was tested and explained in Table 5, the routine can filter out unwanted types of events (tectonic events, in test example) while preferring, e.g., magmatic DLF events (Tables 4 and 5). The main detection restriction in this configuration is the level of signal amplitude which is influenced by the source strength and seismic attenuation characterising the study region. In our study, we used A6-DFMSD with seismic records obtained up to 50 km away from the seismic target centre for events with magnitudes below $ML \sim 1$.

From station to station, the recorded waveforms of a single event vary. This issue becomes evident when nearby seismicity is monitored by a local network, because the source mechanism (radiation pattern) might play a more effective role in comparison with the medium properties and site conditions (site effects). A6-DFMSD is designed to cope with these circumstances by applying two techniques: one applied in the frequency domain and the other in the time domain. In the frequency domain, it calculates the variation coefficient of DFs of the signal, which is a stable criterion for the signals recorded at different stations and emitted from the same source. In this domain, the range of coherency acceptance for the variation coefficient of DFs is individually determined depending on the intensity of the variation coefficient of DFs of each event. In the time domain, it calculates sets of station-wise time limits while searching for coherencies across stations. These time limits are unique for each pair of recording stations and vary depending on the position of each pair of stations relative to the position of the defined target zone, thus searching for a wave front. These time limits are chosen wide enough to include the P- and S-phase pulses. This spread in time allows the detector to decide whether the detected pulses are also observed at neighbouring stations and whether the signals are connected to the same source in the seismic target zone or not. This is done by considering both P- and S-phases into the decision process. By this means, the detector can recognize that the detected pulses are connected to the same event, even if the emitted signal from a source located in the seismic target zone is affected by a strong radiation pattern for which, for example, at one station only the P-phase is detectable and at the other station only the S-phase.

The goal of A6-DFMSD is to not miss the events occurring inside a predefined target region, however, ~50% of our detections belong to distant sources (sources located outside the target region) when the detection of LF events is the goal. This happens because far-distant events have similar signal characteristics, partly in the time domain (waveforms) and mostly in the frequency domain compared with the signals of LF events. These far-distant signals arrive at the network almost simultaneously due to their steep incidence angles and contain lower frequencies as their higher frequency parts are lost due to attenuation.

As a result of the detection mechanism in A6-DFMSD, detection of relatively weak events is enhanced in the regions where the seismological network is denser. If the seismological network is close to cities or industrial regions, the denser part of the network has the main role in detection of incoherent events due to human activities (traffic, industry). To reduce number of the false or human-made (unwanted) events in the detection list we recommend to not use data of the stations with an interstation distance of less than ~2 km to avoid coherent noise signals. For regions, where a 1-D layered seismic velocity model is not yet determined, users can take a 1-D homogenous seismic or a simple 1-D layered seismic velocity model obtained from regions with a similar geology. The output of the detector provides an initial information about the dominant frequency of the detected events which is very useful when searching for a specific type of signal (for example DLF events as in the test example).

To use A6-DFMSD for other targets, beside adding the input information (see Sect. on Input parameters) to the control file of the detector, only the following parameters might require some adjustments (for more details see the Supplementary file). Similar to the role of the detection threshold in STA/LTA, in A6-DFMSD the parameter sigClasPower controls the sensitivity of the detection in respect with the signal to noise ratio. Higher

values for sigClasPower lead to an elimination of weak signal anomalies. On the other hand, lower values than 2 add more incoherent detections. A coherency search in space is limited to a certain number of orbit stations, however, the latter may be adjusted. Therefore, if coherent signal anomalies are found with a minimum number of X stations out of Y orbit stations, this leads to a detection. By increasing the number of Y, while keeping a fixed value for X, a larger radius in space (wider area) is used for finding coherent signal anomalies. This change increases a chance of detecting events which are coherent in their signal properties. By increasing the number of X, while keeping a fixed value for Y, the coherency search performs with a more restricted condition and this leads to the elimination of weaker events. This happens, e.g., due to the wave propagation attenuation which can damp weak signals at larger distances. Indeed, one should always consider that the detection of signals from weak events is limited to a certain hypocentral distance (Li et al. 2020) which might be less than the dynamic search radius defined by the selection of the value Y and the actual station distribution. The values for X and Y are set in the control file as parameters "minLocSearCohStNum" and "maxLocSearStNum", respectively. We recommend to select the values for these two parameters with a ratio of minLocSearCohStNum to maxLocSearStNum between 0.6 and 0.7. Search vicinities around the variation coefficient of DF signal anomalies are determined by empirical Eqs. (6) and (7). These equations were obtained by testing different sets of values and relationships (see also Supplementary material with examples, Sect. 1.5.2 Figs. S5 and S6). Further tries with more datasets may provide an improved performance of the detection. The rest of the parameters introduced in this method are fixed parameters and independent of the target. Changing their values might require an updated regularization step which can lead to changes in the choice of the other adjustable parameters.

The variation coefficient of DFs is a dimensionless value. If the amplitude of the seismic records is multiplied by a value, it does not change the value of the variation coefficient of DFs. Therefore, even records measured at stations located on very different site conditions (where the recorded amplitudes are amplified by some factors due to the site effect) still can be used as input for the detector. We assign this as a stabilising property which becomes important while searching for the correlation between signal anomalies at different stations.

One of the interesting aspects of the detector is the detection of a sequence of events in which the coda of the first event is partly or mostly covered by the phases of the second event and so on. Figure 7 (b and d), Fig. 8 (e and j) and Fig. 9 (a and b) present waveform examples of these type of events with both magmatic and tectonic origins. The recorded waveforms of such sequences are affected by the source activity rate. Such kind of events are typically missed using methods like waveform matching. A6-DFMSD can successfully detect such swarm-like events (or multi-rupture sources). This demonstrates the capability of the method, e.g., for the detection of the tremor-like magmatic signals. Like for the STA/LTA method, such a kind of sequences is also listed as one event but with a difference: A6-DFMSD provides a value in the detection list that gives the time duration between the detection of the first detected phase of the first event in the sequence and the last detected phase of the last event in the sequence, in a network-wide scale. Single events in the detection list have a relatively short time duration (in our test example with an average time duration value of ~ 11 s) whereas sequences of events (including also events outside of the target region, e.g. regional or teleseismic events) have a longer time duration. Hence, one can use this average time duration as a criterium and split the events of the detection list into two groups: the one which mostly contains of single events and the other one which contains sequences of events or events outside the target region. Of course, the average time duration of single events is a function of the network geometry (network diameter), size of the target region (diameter and depth of the target region) and the relative position of the centre of the target region and the centre of the network stations.

In the detection summary (Table 4), we presented a part of the detection output which is generated based on coherent findings at five or more stations in the EEVF. There, we did not take into account the remaining events detected by less than five stations, because the ratio of false detections to the total number of detections increases too much. One suggestion to prevent an increase in false detections is reducing the radius of the target region. Thus, defining a large target region increases the ratio of false detections to the total number of detections. In this study we considered a radius of 25 km for the target region. As result of applying a smaller radius (for example 10 km), the time-window search for finding coherencies is shortened. Consequently, the search with a shorter time-window reduces the chance of the occurrence of false coherent coincidences due to noise signals.

A6-DFMSD can detect a wide range of different signal types. Figures 8 and 9 present the capability of detecting diverse waveforms. These two figures summarize some typical waveform examples of different event types which were detected by A6-DFMSD in the EEVF, not only within the five-month period of the test example, but also since starting the DEEP-TEE project in July

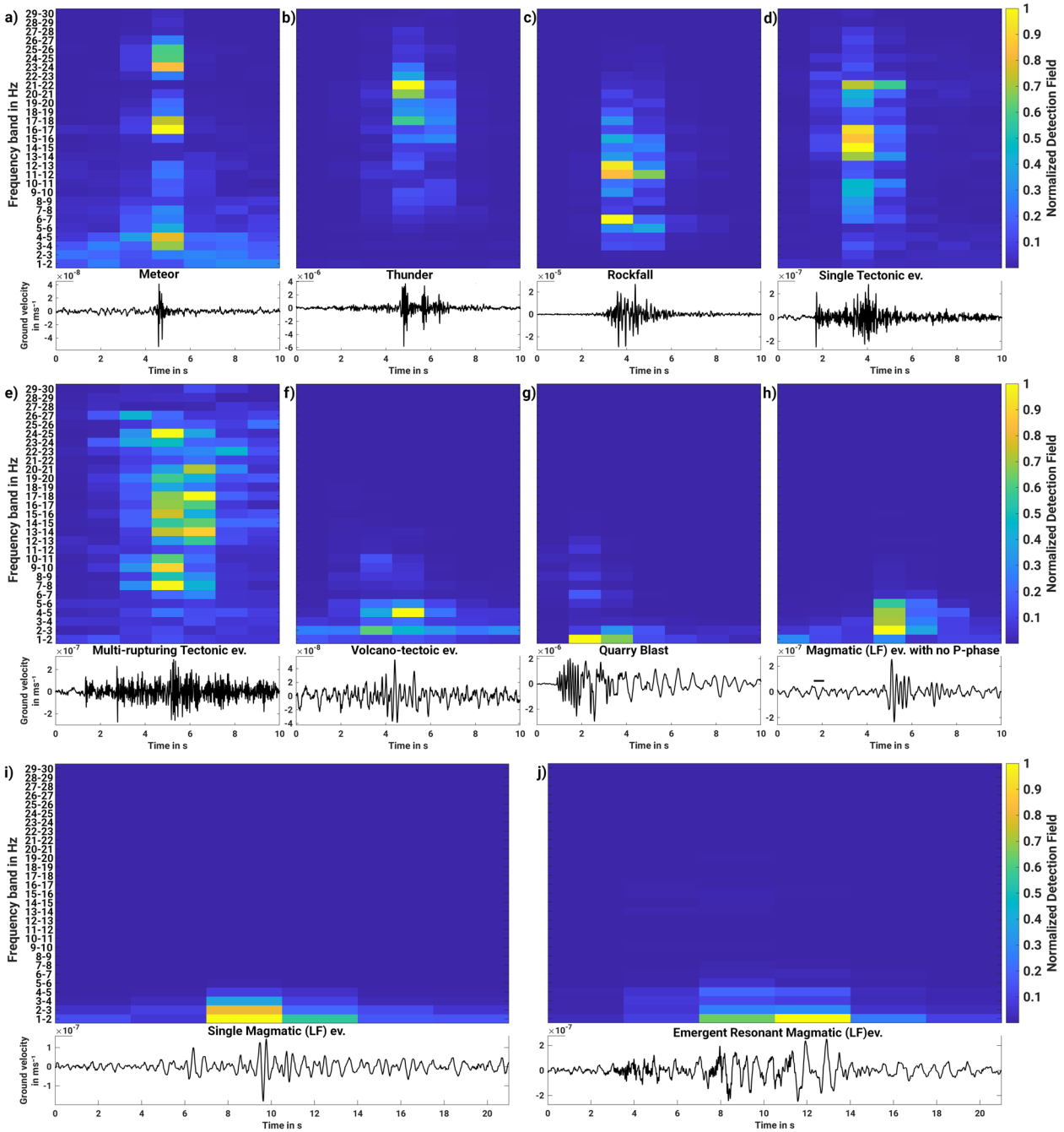


**Fig. 8** Waveform examples (ground motion velocity, vertical component) along with their corresponding detection fields (windowed energy-proportional narrow bands, similar to Fig. 5f, but as spectrogram) for different event types detected by A6-DFMSD in the EEVF. Records in the subplots are in UTC since: (**a**) 2016-08-08T00:06:54.50 at DEP12, (**b**) 2015-08-10T19:55:19.00 at DEP02, (**c**) 2020-10-20T02:20:06.50 at OF09, (**d**) 2018-01-31T22:48:27.50 at DEP12, (**e**) 2020-07-03T05:48:03.00 at GLOK, (**f**) 2018-02-18T02:01:46.00 at LAGB, (**g**) 2020-10-05T09:18:24.00 at OCHT, (**h**) 2017-06-06T19:22:06.00 at LAGB, (**i**) 2017-06-04T20:36:32.00 at LAGB, and (**j**) 2018-04-28T02:44:58.00 at DEP12

2014. In Fig. 8, atmospheric signals are presented under the labels "Thunder" and "Meteor". We identified several hundreds of thunders and even some bursts of meteors around our seismological station network (Eickhoff et al. 2024). The location of these type of signals, up to tens of kilometers high in the atmosphere, is verified by source location using a sound velocity model of the atmosphere (Kirtskhalia 2012).

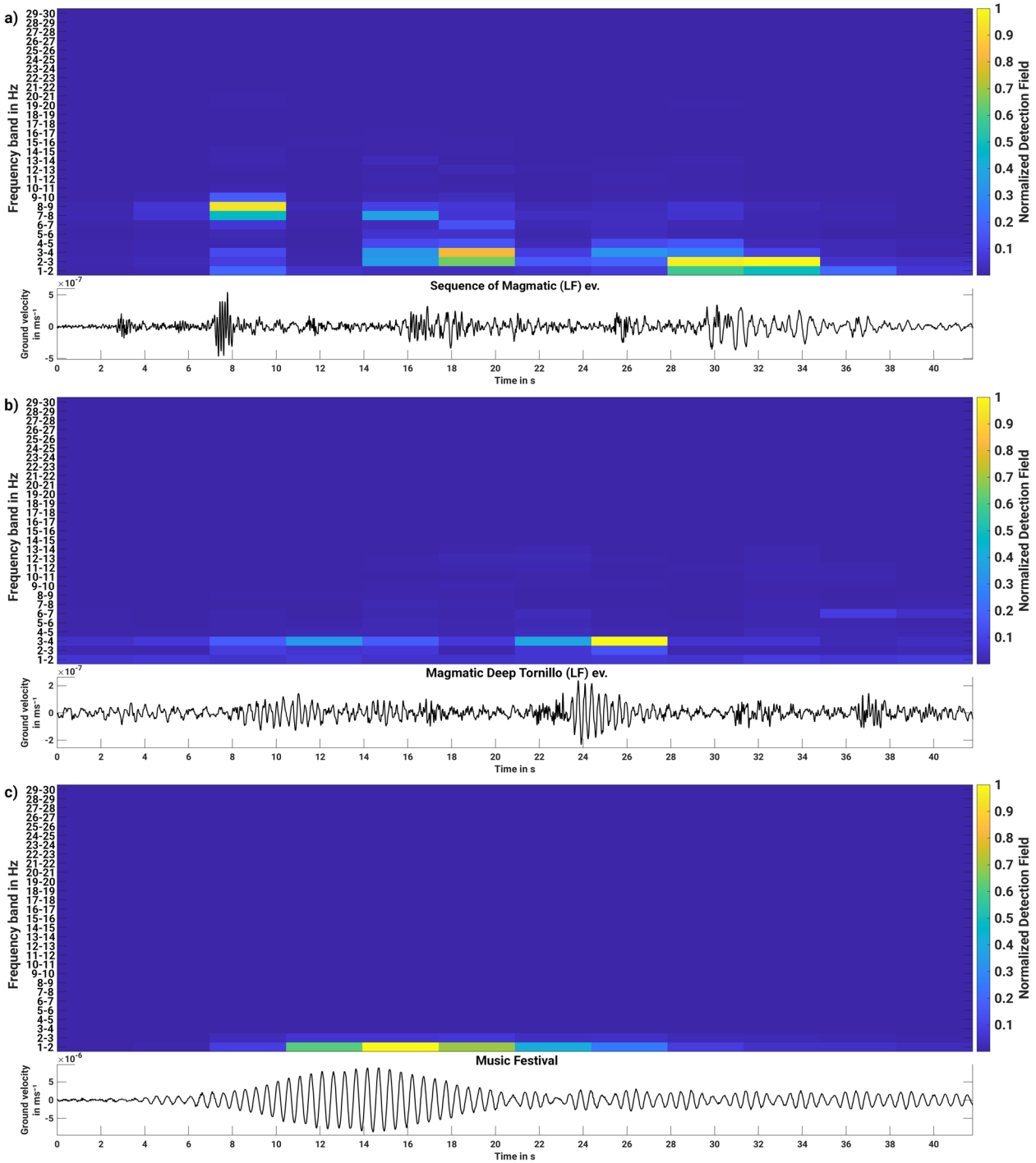


**Fig. 9** Waveform examples (ground motion velocity, vertical component) along with their corresponding detection fields (windowed energy-proportional narrow bands, similar to Fig. 5f, but as spectrogram) for different event types detected by A6-DFMSD in the EEVF. Note: the signal from the music festival is similar to magmatic tornillo-shaped LF events (see e.g., Wassermann 2012). Records in the subplots are in UTC since: (a) 2019-08-07T21:13:44.20 at GLOK, (b) 2019-04-08T20:08:05.00 at DEP08 and (c) 2015-06-05T21:10:45.00 at DEP09

Quarry blast signals are the most common and often strongest anthropogenic signals. In Fig. 8, one example is presented under the label "Quarry blast". In our study, detection of quarry blast signals is limited to day-time (7:15–15:15 UTC). Since the frequency content of the quarry blasts totally overlaps with the frequency content

of the LF events, they are the most frequent detections during day-time (see explanation of the Tables 4 and 5 for more details). This type of the events is also labelled by the frequency classes 1 to 3 in the detection lists, similar to the label setting of the LF evens. For this reason, the current version of A6-DFMSD is not completely able to distinguish the LF events from quarry blasts. We note that up to a radius of 100 km from the centre of the target region in the EEVF, we could identify the locations of 424 open mines using Google Maps. This demonstrates the challenging conditions regarding the detection of LF events in our target region where anthropogenic noise is very high. Another anthropogenic signal that is interesting from the detection point of view are some sets of long-lasting signals emitted from a music festival hold in May 2015 in the EEVF, called *Rock am Ring* (Fig. 9 the signal labelled by "Music festival"). These signals are prominent in the frequency band 1–5 Hz, with a high peak at 2 Hz. Both, the waveform and the frequency content are similar to volcanic tremor (e.g., Wassermann 2012), however the shallow hypocentre, the location and the origin time are coincident with the *Rock am Ring* festival and, therefore, excluding a magmatic origin. The signal labelled by "Rockfall" in Fig. 8 is detected during midnight (local time) with a shallow (~0.1 km depth) source position, matching with the location of a big open mine in the region. The waveform characteristics of this event do not match with the waveforms of the other type of observed events in the region. Since blasting in the mines is limited to day time, falling rocks at midnight inside the open mine is the most reasonable scenario explaining the detected observed signal.

The most ordinary type of the LF signals observed in EEVF is shown in Fig. 8 with the label "Single Magmatic ev.". Relative to the other waveforms of the observed LF signals in EEVF, this type of signals has a shorter duration. Their occurrence is not limited in a certain depth location. Depending on the relative source-station position, noise level and magnitude of the event, the P-phase might not be seen in the records. One example of this kind of observed signal is labelled by "Magmatic ev. with no P phase" in Fig. 8. There, the expected P-phase arrival time is marked by a "-" after localization of the event with the useable picked phases taken at the DEEP-TEE network stations. Among the detected signals of the LF events in the EEVF, there are some signals that provide evidence for the occurrence of resonance (in Fig. 8, "Emergent Resonant Magmatic ev."). This type of signals starts with a small amplitude, comparable with the background noise, and then the lower frequency part of the signal is gradually increasing over time at all the network stations. This type of event occurs in a shallow position (~10 km depth). In Fig. 9 two of the most interesting types of the long-lasting magmatic signals are presented, too. The source of both events is located deeply below the Moho at ~39 km and ~33 km depth, respectively. The first one is a sequence of events in which the frequency content of the events decreases in time (Fig. 9a). This characteristic of the sequence is well illustrated in the detection fields plotted below the signal. The observation of such kind of signals was already reported by Aki et al. (1977) from Kilauea volcano, Hawaii. Aki and Koyanagi (1981) modelled the mechanical mechanism as magmatic intrusions, explaining the characteristics of the signal. The second example in Fig. 9b is a pulse-like signal very similar to long-lasting magmatic LF events which sometimes are called tornillos. The related detection fields of this event illustrate the partly mono-chromatic frequency behaviour. This example shows, even if these signals are characterised by a lower amplitude than other higher frequency signals, the frequency domain part of A6-DFMSD will facilitate their detection.

## Conclusion and outlook

We introduce a seismic event detector (A6-DFMSD) which is able to detect local (micro-) seismic events occurring inside an arbitrary target zone in the presence of a moderate to high local seismic noise level. It is sensitive to the energy increase in the continuous ground motion in the frequency and time domains and it does not require a priori knowledge of the waveform characteristics of the searched events. Station coordinates, location and cylindric geometry of a seismic target zone and an approximate simple 1-D (homogeneous or layered) seismic velocity model of the region are the only input that is required to apply A6-DFMSD on a seismic dataset.

To evaluate the method, we selected 5 months of continuous seismic records in the East Eifel Volcanic Field (EEVF), Germany, which is a challenging test example, because (a) different types of seismic sources (with magmatic and tectonic origins) have already been identified (Hensch et al. 2019) and (b) there is a high cultural noise level in the records. All the detected events were manually checked by visual inspection of the waveforms, localized and classified. Results were then compared with a merged list of three local seismicity catalogues (Table 4) and also with the results of STA/LTA tuned for detection of DLF events (Table 5). In comparison with the merged list of three local seismicity catalogues and regarding the detection of all type of natural source events (e.g., DLF, tectonic and volcano-tectonic), A6-DFMSD detected 4.3 times more events without missing any tectonic or DLF event.

In comparison with the results of STA/LTA tuned for detection of DLF events, A6-DFMSD and STA/LTA,

both, detected the same number of DLF events. However, the STA/LTA results included 3.7 and 1.3 times more false detections in comparison with A6-DFMSD where the high sensitive event lists (set A and set A´) and the low sensitive event lists (set B and set B´) are taken into consideration, respectively (Table 5). It is noteworthy that STA/LTA results included 27 and 15.3 times more tectonic type events than A6-DFMSD (comparing set A with set A´, and set B with set B´, respectively), although for both methods the detection of DLF events was the goal. This comparison shows that besides the task of detection, A6-DFMSD can successfully separate events concerning their frequency content. In this regard, the separation of quarry blasts from LF events still remains as an unsolved issue, due to the fact that quarry blasts and LF events are characterised by very similar features in frequency domain.

Based on the detection mechanisms implemented in A6-DFMSD, the following cases are the most recommended targets for applying the method:

a) regions which are newly covered by a local seismological network (or, when the local seismological network is still under development), especially, if no local waveforms are known,
b) detection of new types of seismic sources with unknown waveforms,
c) if waveform matching detection methods are planned but reference waveforms are not yet identified.

In the latter case (c), A6-DFMSD is recommended as a pre-detection step. In this case, A6-DFMSD provides a diverse set of waveforms as inputs for waveform matching detection methods and prevents these methods from missing events in their blind spots.

All coding is currently done in one MATLAB program. However, users are free to connect optional routines. For example, users may integrate the TauP Toolkit for the travel time calculation as well. Similarly, a preferred location routine can be added to the detection part.

## Supplementary Information

The online version contains supplementary material available at https://doi.org/10.1186/s13617-024-00147-8.

Supplementary Material 1.

**Acknowledgements**
We thank Dr. Hans Agurto Detzel for the thorough reading of our manuscript and advice. The waveforms of the DEEP-TEE experiment were provided by the datacenters of the KArlsruhe BroadBand Array (KABBA), GFZ Potsdam, https://geofon.gfz-potsdam.de/doi/network/1P/2014 and the State Seismological Services of the states of Rhineland-Palatinate and North Rhine-Westphalia. Temporary recording stations were borrowed from the KArlsruhe BroadBand Array (KABBA) and the Geophysical Instrument Pool at GFZ Potsdam. Detection lists were provided by the State Seismological Service of Baden-Württemberg (Az. 4784//19_12333) and Bensberg Seismological Station, University of Cologne, http://www.seismo.uni-koeln.de/catalog/index.htm. Maps are plotted with GMT (Wessel et al., 2019). K.K. is supported with a grant from the Ministry of Science, Research and Arts Baden-Württemberg and had a grant from the STIBET DAAD Pre-Graduation Scholarship. Four anonymous reviewers helped to improve and clarify the manuscript.

**Authors' contributions**
K.K. coded the computer program, J.R.R.R. did the field experiment, both were writing the text.

**Funding**
Open Access funding enabled and organized by Projekt DEAL. K.K. is supported with a grant from the Ministry of Science, Research and Arts Baden-Württemberg and had a grant from the STIBET DAAD Pre-Graduation Scholarship.

**Data availability**
The data is partly available at GFZ Potsdam at: https://geofon.gfz-potsdam.de/doi/network/1P/2014. The code is available at GitHub (https://github.com/Koushesh/A6-DFMSD/tree/master). A user manual description for the potential users will be available at GitHub after acceptance of the manuscript.

## Declarations

**Ethics approval and consent to participate**
Not applicable.

**Consent for publication**
Not applicable.

**Competing interests**
The authors declare no competing interests.

Received: 13 November 2023 Accepted: 10 October 2024
Published online: 24 October 2024

**References**

Aki K, Koyanagi R (1981) Deep volcanic tremor and magma ascent mechanism under Kilauea, Hawaii. J Geophys Res 86:7095–7109
Aki K, Fehler M, Das S (1977) Source mechanism of volcanic tremor: fluid-driven crack models and their application to the 1963 Kilauea eruption. J Volcanol Geoth Res 2:259–287
Allen RV (1978) Automatic earthquake recognition and timing from single traces. Bull Seismol Soc Am. https://doi.org/10.1785/bssa0680051521
Bean CJ, De Barros L, Lokmer I, Métaxian J-P, O' Brien G, Murphy S (2014) Long-period seismicity in the shallow volcanic edifice formed from slow-rupture earthquakes. Nat Geosci 7:71–75
Bensberg Observatory, University of Cologne (2023) http://www.seismo.uni-koeln.de/events/index.htm . Accessed 17 Apr. 2023
Chouet BA (1988) Resonance of a fluid-driven crack: Radiation properties and implications for the source of long-period events and harmonic tremor. J Geophys Res 93:4373–4400
Cusano P, Petrosino S, Bianco F, Del Pezzo E (2013) The first long period earthquake detected in the background seismicity at Mt. Vesuvius Annals Geophys 56(4):S0440. https://doi.org/10.4401/ag-6447
Eickhoff D, Föst J-P, Ostermeier R, Koushesh M, Ritter JRR (2024) Estimating a meteoroid's trajectory using seismic data: a case study of the November 2017 meteoroid over Germany. Proceedings of the International Meteor Conference Redu, Belgium, 2023, 143–145, ISBN 978-2-87355-036-3
Gal F, Brach M, Braibant G, Jouin F, Michel K (2011) $CO_2$ escapes in the Laacher see region, East Eifel, Germany: application of natural analogue onshore and offshore geochemical monitoring. Int J Greenhouse Gas Control 5:1099–1118
Hensch M, Dahm T, Ritter J, Heimann S, Schmidt B, Stange S, Lehmann K (2019) Deep low frequency earthquakes reveal ongoing magmatic

recharge beneath Laacher See Volcano (Eifel, Germany). Geophys J Int 216:2025–2036
Hidayat D, Voight B, Langston C, Ratdomopurbo A, Ebeling C (2000) Broadband seismic experiment at Merapi Volcano, Java, Indonesia: very-long-period pulses embedded in multiphase earthquakes. J Volcanol Geoth Res 100:215–231
Kirtskhalia VG (2012) Speed of sound in atmosphere of the earth. Open J Acoust 2:80–85
Kissling E, Ellsworth WL, Eberhart-Phillips D, Kradolfer U (1994) Initial reference models in local earthquake tomography. J Geophys Res 99:19635–19646
Kreemer C, Blewitt G, Davis PM (2020) Geodetic evidence for a buoyant mantle plume beneath the Eifel volcanic area, NW Europe. Geophys J Int 222:1316–1332. https://doi.org/10.1093/gji/ggaa227
Li L, Tan J, Schwarz B, Staněk F, Poiata N, Shi P, Diekmann L, Eisner L, Gajewski D (2020) Recent advances and challenges of Waveform-based seismic location methods at multiple scales. Rev Geophys 58(e2019RG000667). https://doi.org/10.1029/2019RG000667
Malfante M, Dalla Mura M, Metaxian J-P, Mars J, Macedo O, Inza A (2018) Machine learning for volcano-seismic signals: challenges and perspectives. IEEE Signal Process Magazine Inst Electr Electron Eng 35:20–30
Naofumi A, Kazuaki O, Satoshi I (2013) Tectonic, volcanic, and semi-volcanic deep low-frequency earthquakes in western Japan. Tectonophysics 600:27–40
Neuberg JW (2011) Earthquakes, Volcanogenic. In: Gupta HK (ed) Encyclopedia of Solid Earth Geophysics. Encyclopedia of Earth Sciences Series. Springer, Dordrecht. https://doi.org/10.1007/978-90-481-8702-7_159.
Neuberg J, Luckett R, Baptie B, Olsen K (2000) Models of tremor and low-frequency earthquake swarms on Montserrat. J Volcanol Geoth Res 101:83–104
Perol T, Gharbi M, Denolle M (2018) Convolutional neural network for earthquake detection and location. Sci Adv 4(2). https://doi.org/10.1126/sciadv.1700578
Ratdomopurbo A, Poupinet G (2000) An overview of the seismicity of merapi volcano (java, Indonesia), 1983–1994. J Volcanol Geoth Res 100:193–214
Reinig F, Wacker L, Jöris O, Oppenheimer C, Guidobaldi G, Nievergelt D, Adolphi F, Cherubini P, Engels S, Esper J, Land A, Lane C, Pfanz H, Remmele S, Sigl M, Sookdeo A, Büntgen U (2021) Precise date for the Laacher see eruption synchronizes the younger Dryas. Nature 595:66–69. https://doi.org/10.1038/s41586-021-03608-x
Ritter JRR (2007) The seismic signature of the Eifel Plume. In: Ritter JRR, Christensen UR (eds) Mantle plumes. Springer, Berlin, Heidelberg. https://doi.org/10.1007/978-3-540-68046-8_12.
Ritter JRR, Koushesh K, Schmidt B, Bühler J, Föst J-P, Hensch M, Mader S (2024) Seismological Monitoring of Magmatic and Tectonic Earthquakes in the East Eifel Volcanic Field (eds) Germany. Journal of Seismology (in print)
Ritter JR, Jordan M, Christensen UR, Achauer U (2001) A mantle plume below the Eifel volcanic fields, Germany. Earth Planet Sci Lett 186:7–14
Ross ZE, Trugman DT, Hauksson E, Shearer PM (2019) Searching for hidden earthquakes in Southern California. Science 364:767–771
Schmincke H-U, Lorenz V, Seck HA (1983) The Quarternary Eifel volcanic fields. In: Fuchs K, Gehlen KV, Mälzer H, Murawski H, Semmel A: Plateau uplift. The Rhenish Shield — a case history, 139–151, Springer, Berlin, Heidelberg, New York, Tokyo
Schmitt AK, Wetzel F, Cooper KM, Zou H, Wörner G (2010) Magmatic longevity of Laacher see volcano (Eifel, Germany) indicated by U-Th dating of intrusive carbonatites. J Petrol 51:1053–1085
Sherburn S, Scott BJ, Nishi Y, Sugihara M (1998) Seismicity at white island volcano, New Zealand: a revised classification and inferences about source mechanism. J Volcanol Geoth Res 83:287–312
Stange S, Kurrle D, Dahm T, Hinzen K-G, Lehmann K, Ritter JRR, Schmidt B (2014) Subkrustale Seismizität in der Osteifel, in Proceedings of the Annual Meeting of the German Geophysical Society (Abstract S-5.002)
State seismological service of Rhineland-Palatinate (2023) https://www.lgb-rlp.de/de/fachthemen-des-amtes/landeserdbebendienst-rheinland-pfalz/. Accessed 3 Nov. 2023
Stroujkova A, Malin P (2001) Multiple ruptures for long valley microearthquakes: a link to volcanic tremor. J Volcanol Geoth Res 106:123–143
Trnkoczy A (2009) Understanding and parameter setting of STA/LTA trigger algorithm. – In: Bormann P (ed) New Mannual of Seismological Observatory Practice (NMSOP), Potsdam, Deutsches GeoForschungsZentrum GFZ, 1:20
Wassermann J (2012) Volcano seismology. -. In: Bormann P (ed) New Manual of Seismological Observatory Practice 2 (NMSOP-2). Deutsches GeoForschungsZentrum GFZ, Potsdam, pp 1–77. https://doi.org/10.2312/GFZ.NMSOP-2_ch13. Accessed 3 Nov. 2023
Wörner G, Wright TL (1984) Evidence for magma mixing within the Laacher see magma chamber (East Eifel, Germany). J Volcanol Geoth Res 22:301–327
Yoon CE, O'Reilly O, Bergen KJ, Beroza GC (2015) Earthquake detection through computationally efficient similarity search. Sci Adv 1(11). https://doi.org/10.1126/sciadv.1501057

## Publisher's note